Thin Solid Films 807 (2024) 140548

Contents lists available at ScienceDirect

Thin Solid Films

journal homepage: www.elsevier.com/locate/tsf

Compositional changes between metastable SnO and stable SnO_2 in a sputtered film for p-type thin-film transistors

Yong-Lie Sun [a], Toshihide Nabatame [a,*], Jong Won Chung [b], Tomomi Sawada [a], Hiromi Miura [a], Manami Miyamoto [a], Kazuhito Tsukagoshi [a,*]

[a] Research Center for Materials Nanoarchitectonics, National Institute for Materials Science, Tsukuba 305-0044, Japan
[b] Samsung Advanced Institute of Technology (SAIT), Samsung Electronics, Suwon 16678, South Korea

ARTICLE INFO

Keywords:
p-Type SnO
Tin oxide
Thin-film transistors
Sputtering
High vacuum annealing

ABSTRACT

p-Type tin(II) oxide (SnO (Sn^{2+})) formation using radiofrequency (RF) reactive magnetron sputtering and post-deposition annealing (PDA) processes was investigated. The as-grown SnO_x film deposited from an SnO_x (SnO:Sn = 60:40) target by RF sputtering at an oxygen partial pressure (P_{O2}) of 0 Pa consisted of 2 % Sn (Sn^0), 42 % Sn^{2+}, and 56 % SnO_2 (Sn^{4+}). However, compared with the Sn^{2+} fraction observed after PDA under N_2 and low-vacuum (~1 Pa) conditions, that after PDA at 300 °C under high vacuum ($< 5 \times 10^{-4}$ Pa) (HVPDA) increased substantially to greater than 62 %. This result was attributed to the transformation from SnO_2 to SnO during HVPDA. A staggered bottom-gate thin-film transistor with an SnO channel (10 nm), which was fabricated by HVPDA at 300 °C, exhibited p-type properties, including a relatively high on-current/off-current (I_{on}/I_{off}) ratio of 5.1×10^4 and a hole field-effect mobility (μ_{FE}) of 1.8 $cm^2/(V \cdot s)$.

1. Introduction

n-Type oxide semiconductors stand out in cutting-edge electronic applications because of their high mobility, low off-current, and good compatibility with low-temperature fabrication methods. These materials have therefore been identified as highly promising semiconductors for use in advanced displays, sensors, and ferroelectric transistor channels [1-5]. Numerous In_2O_3-based oxide semiconductors, including In_2O_3, C-doped In_2O_3, In–Si–O, In–W–O, and In–Ga–Zn–O, have been widely investigated as n-type oxide semiconductors [6-10].

The development of p-type oxide semiconductors, such as tin(II) oxide (SnO), nickel(II) oxide (NiO), and copper(II) oxide (CuO), continues to encounter problems related to low hole mobility and poor reliability [11,12]. Among these materials, SnO has emerged as a notable p-type oxide semiconductor; however, achieving both high field-effect mobility (μ_{FE}) and a large I_{on}/I_{off} ratio in SnO-based thin-film transistors (TFTs) is challenging because SnO (Sn^{2+}) is a thermodynamically metastable phase [13-21]. Its metastability often leads to the formation of n-type SnO_2 (Sn^{4+}) or other intermediate phases such as Sn_2O_3 or Sn_3O_4, and sometimes phase-pure residual metallic Sn (Sn^0), resulting in the coexistence of both p-type SnO and n-type phases and further degradation of device efficiency [18-20,22,23]. Thus, the fabrication of stable p-type SnO by controlling the deposition and post-deposition annealing (PDA) conditions is important. p-Type SnO films have typically been fabricated using two reaction methods. SnO has been predominantly fabricated by oxidizing a deposited film composed of Sn-rich SnO_x and Sn [24,25]. As a minority phase, SnO was formed via decomposition of SnO_2 [26].

Metallic Sn [19,27], ceramic SnO [20,27–30] and SnO_2 [31,32], and Sn+SnO_2 [33,34] and Sn+SnO [35] mixtures have been used as targets in sputtering methods. As-grown SnO films are expected to have a stoichiometric O/Sn ratio of 1/1 and a large SnO fraction. Metallic Sn targets are limited by their low melting point and the narrow processing window for oxygen partial pressure and sputtering power during sputtering of pure SnO films [19,35]. A pure SnO_2 target predominantly forms n-type SnO_2 because O–Sn–O bonds involving Sn^{4+} are more stable than those involving Sn^{2+} particularly at high-temperature. Meanwhile, sputtering targets with mixtures of metals and ceramics offer both reliable film production and an enlarged processing window, making their use a promising approach for attaining stable and manageable p-type SnO thin films.

The effect of the annealing atmosphere and temperature during post-deposition annealing (PDA) of SnO films has also been studied. Lin *et al.* explored how SnO films react to annealing under various atmospheres

* Corresponding authors.
E-mail addresses: nabatame.toshihide@nims.go.jp (T. Nabatame), tsukagoshi.kazuhito@nims.go.jp (K. Tsukagoshi).

https://doi.org/10.1016/j.tsf.2024.140548
Received 5 May 2024; Received in revised form 30 September 2024; Accepted 6 October 2024
Available online 9 October 2024
0040-6090/© 2024 The Author(s). Published by Elsevier B.V. This is an open access article under the CC BY-NC-ND license (http://creativecommons.org/licenses/by-nc-nd/4.0/).

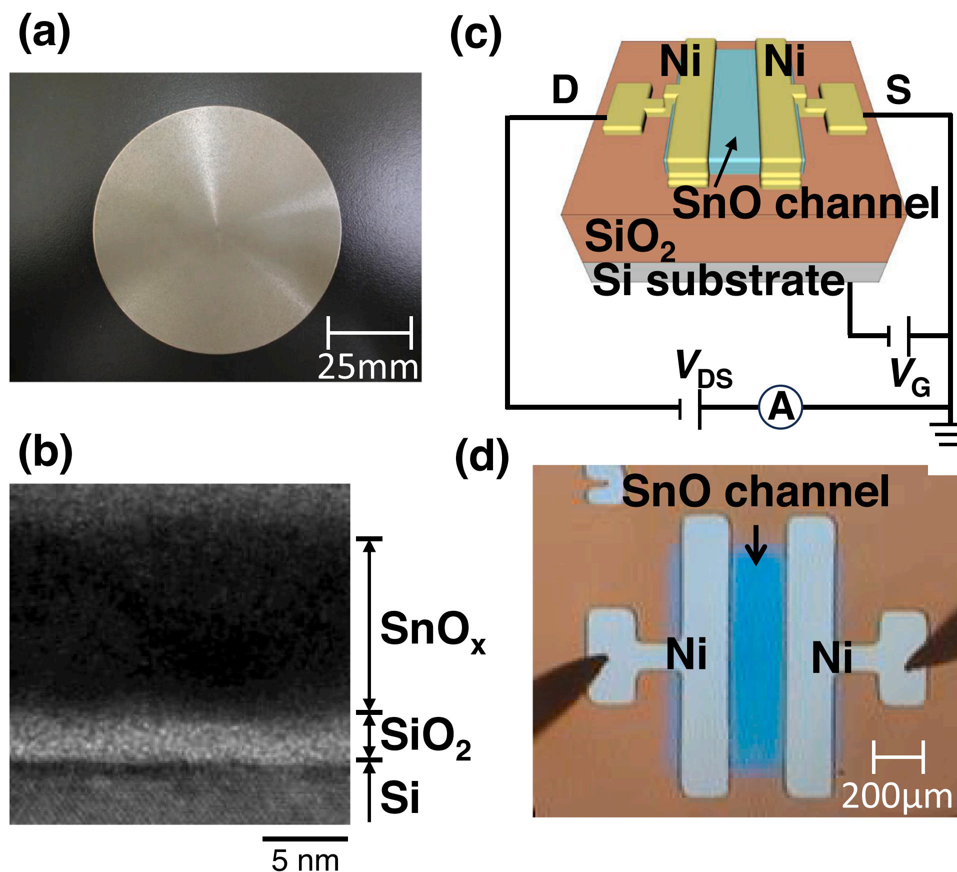

Fig. 1. (a) Photograph of SnO_x target. (b) Cross-sectional TEM image of as-grown SnO_x film deposited at $P_{O2} = 0$ Pa using SnO_x target. (c) Schematic of bottom-gate TFT with SnO channel (Length = 250 µm, Width = 1000 µm) and (d) optical microphotograph of TFT with SnO channel.

(including vacuum, air, O_2, and N_2) over the temperature range 100–500 °C and found that films annealed at 500 °C contained both SnO and SnO_2 phases under all of the tested atmospheres [32]. Contrarily, other researchers have reported attaining single-phase p-type SnO thin films after annealing at 500 °C [36] or even at 600 °C [13] for 30 min in vacuum. Although the atmosphere during PDA is an important factor for forming p-type SnO, the effect of vacuum pressure on SnO is unclear. In addition, the literature contains no reports on the electrical properties of TFTs with an SnO channel formed by PDA under high vacuum.

In the present study, we investigate the effects of sputtering with an SnO_x target (SnO:Sn = 60:40) and PDA under three different atmospheres (N_2 gas, low vacuum (~1 Pa) (LVPDA), and high vacuum ($<5 \times 10^{-4}$ Pa) (HVPDA)) on the formation of p-type SnO. We also demonstrate the transistor performance of SnO-channel staggered bottom-gate TFTs fabricated on p-doped Si substrates with an SiO_2 insulator layer.

2. Experimental methods

2.1. SnO_x film fabrication

The SnO_x films were deposited on p-doped Si substrates (15 × 15 mm) with an SiO_2 layer at room temperature under a deposition power of 125 W via radiofrequency (RF) reactive magnetron sputtering using an SnO_x target (SnO-to-Sn volume ratio of 60:40) (Fig. 1(a)). The target, purchased from Kojundo Chemical Laboratory Co.,Ltd., has a density of 86 % and a size of 3 inches. Unlike conventional ceramic targets, which often contain a binder metal such as Zn, the SnOx target does not contain a binder additive. Then, the SnOx target is composed entirely of Sn and oxygen. The target-to-substrate distance is set to 82 mm. The SiO_2 thickness was 1.5 nm for surface analysis, 200 nm for Hall measurements, and 250 nm for TFT characterization. Here, substrates with 1.5 nm thick SiO_2 is bare Si substrates with a native oxide, substrates with 200 nm and 250 nm thick SiO_2 are thermal oxide Si. The oxygen partial pressure (P_{O2}) was varied from 0 to 0.055 Pa by changing the O_2/Ar gas flow. As-grown SnO_x films deposited at $P_{O2} = 0$ Pa were ~10 nm thick, as determined from a cross-sectional transmission electron image (Fig. 1(b)). The SnO_x films were subsequently annealed by PDA under three different atmospheres: N_2, LVPDA at ~1 Pa, and HVPDA at $<5 \times 10^{-4}$ Pa. PDA was carried out at 300 °C for 60 min. For Hall effect measurements, 10-nm-thick SnO_x films were deposited on p-doped Si/SiO_2 substrates. HVPDA was carried out for 60 nm at a temperature of 200 to 400 °C. Finally, Ni electrodes (100 nm) were formed on the SnO_x films at four diagonal locations through a metal stencil mask. Other SnO_x films were also prepared via direct-current sputtering at room temperature with a metallic Sn target under a sputtering power of 25–50 W and a P_{O2} of 0.025–0.26 Pa.

2.2. p-Type SnO TFT fabrication

Fig. 1(c) shows a back-gate-type TFT with an SnO channel. A 10-nm-thick SnO channel was first deposited on a heavily p-doped Si/SiO_2 substrate through a metal mask under the same RF sputtering conditions using an SnO_x target. HVPDA was then carried out in the temperature range 200–400 °C for 60 min. For ohmic contacts, Ni (100 nm) films were formed as source–drain electrodes through a metal mask by thermal evaporation at room temperature. The channel length (L) was varied from 50 to 350 µm, and the channel width (W) was 1000 µm (Fig. 1(d)).

2.3. Characterization

The crystal structures of the SnO_x films were analyzed using X-ray diffraction (XRD) (Bragg-Brentano geometry) with a Cu Kα radiation

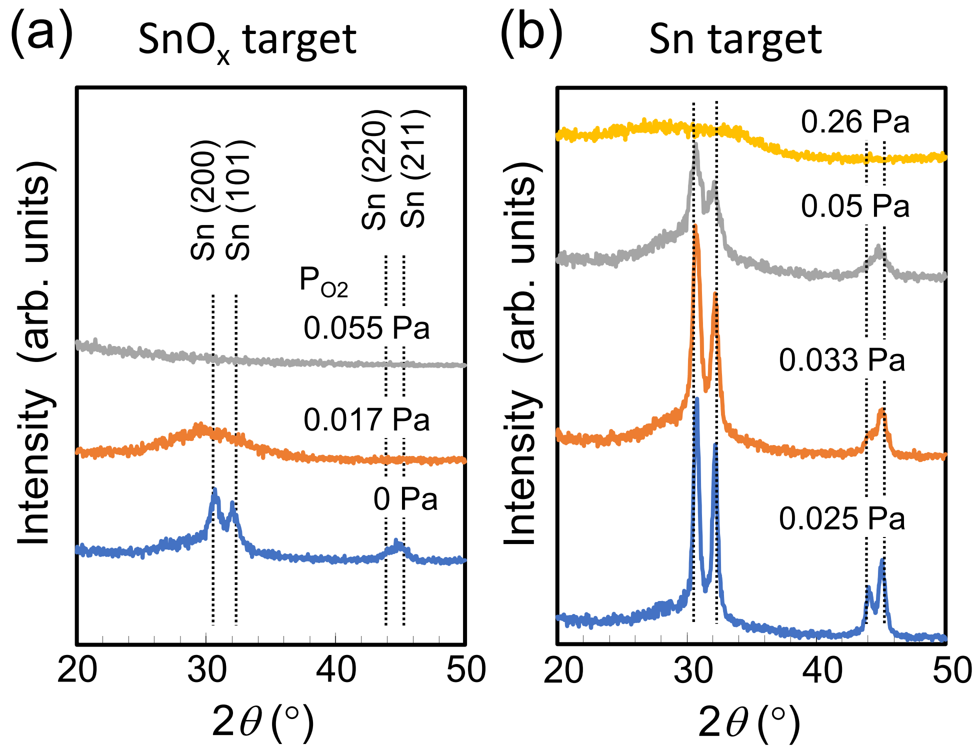

Fig. 2. XRD patterns for as-grown SnO_x films prepared using (a) SnO_x and (b) Sn targets. P_{O2} was varied for each sputtering process.

source (Cu Kα1 1.541Å and Kα2 1.544Å) operating at a voltage of 40 kV and current of 30 mA (SmartLab 3 kW, Rigaku, Japan). The XRD measurement was performed in a low angle X-ray incident configuration with a fixed angle of 1° The chemical binding states were characterized using X-ray photoelectron spectroscopy (XPS) using a monochromatized Al Kα source (1486.6 eV) with a detection area of 100 μmϕ, a detection

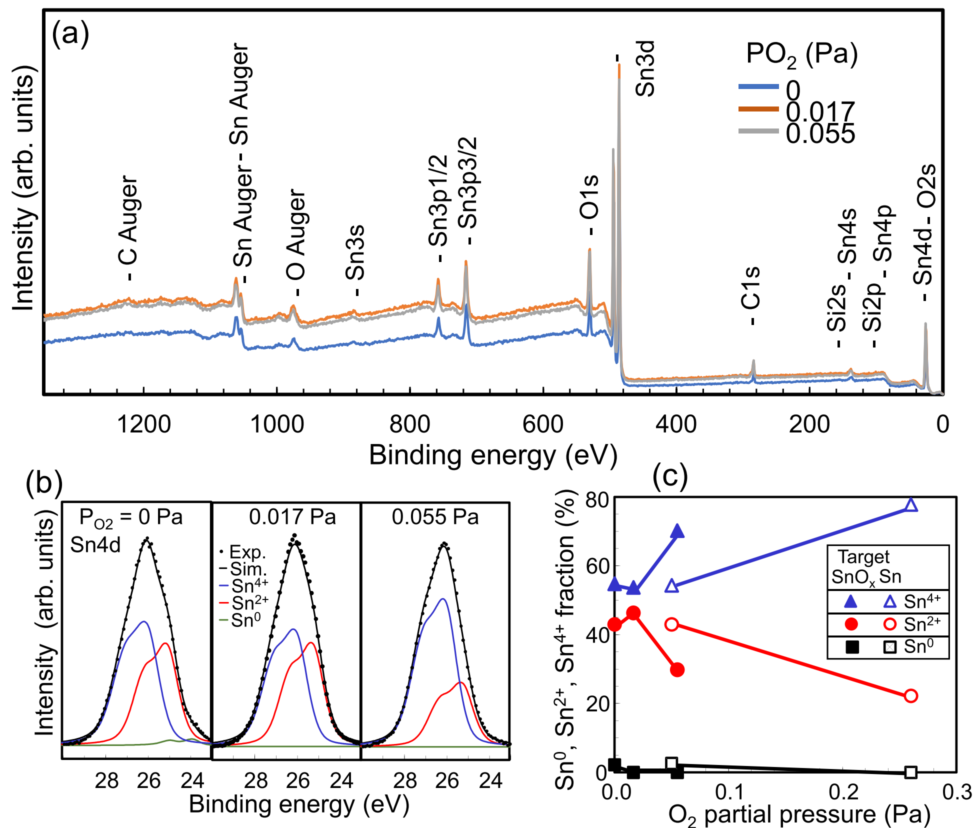

Fig. 3. (a) Wide-scan XPS spectra and (b) Sn 4d XPS spectra of as-grown SnO_x films prepared using SnO_x target. (c) Sn^0, Sn^{2+}, and Sn^{4+} fractions of as-grown SnO_x films as function of P_{O2} during sputtering.

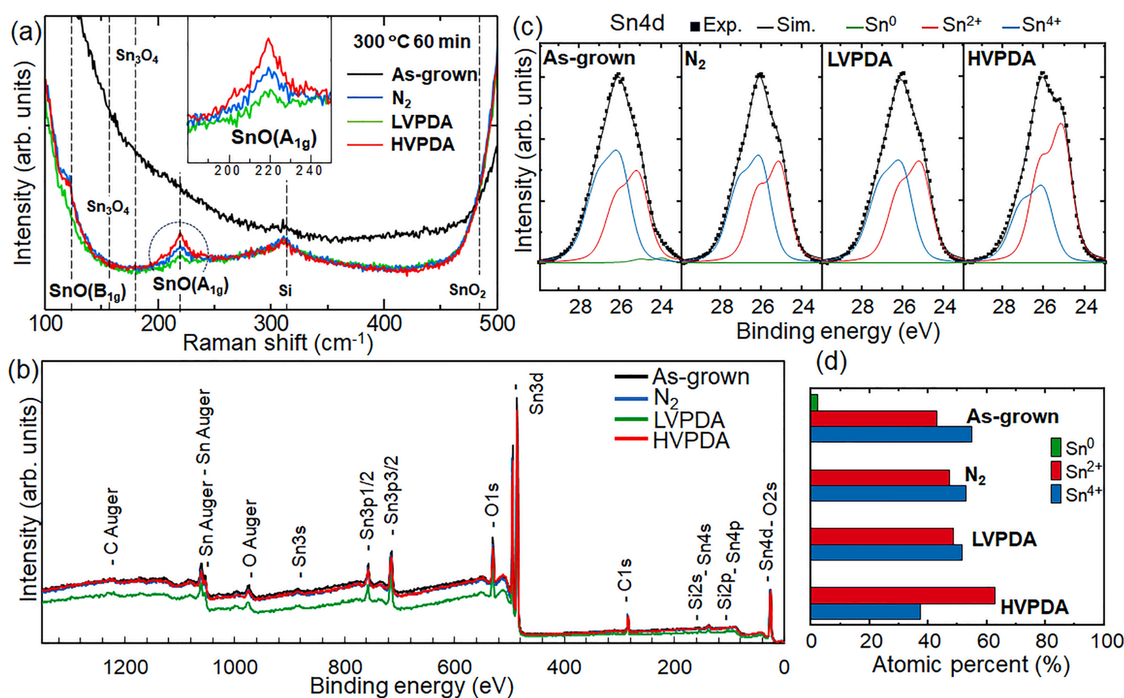

Fig. 4. (a) Raman spectra, (b) wide-scan XPS spectra, (c) XPS 4d spectra, and (d) Sn^0, Sn^{2+}, and Sn^{4+} fractions of as-grown and annealed SnO_x films.

depth of 4–5 nm, a take-off angle of 45°, and a base pressure of ≦5 × 10^{-6} Pa (QuanteraSXM, ULVAC-PHI, Japan). The calibration of XPS binding energy scale was carried out using Au and Cu reference samples and surface sputtering was not performed in this study. XPS peak fitting was performed by the Foundation for Promotion of Material Science and Technology of Japan (MST) with an in-house software with the Shirley background subtraction, and the deconvolution error is claimed to be of ± 3 %. The Raman spectra were collected using a micro-Raman scattering system (Nanofinder FLEX, Tokyo Instruments, Japan) with a 100× objective lens; a green laser (532 nm) was used as the excitation source. Hall mobility, carrier density, and conductivity data were extracted from the results of room-temperature Hall effect measurements conducted using a Hall effect measurement system (HMS-5000, Ecopia, South Korea). Electrical measurements of the SnO TFTs were conducted using a precision semiconductor parameter analyzer (4156C, Keysight Technologies, US) in the dark on a probe station under vacuum. Performance metrics of linear-region μ_{FE}, on-current/off-current (I_{on}/I_{off}) ratio, subthreshold swing (SS), and threshold voltage (V_{TH}) were evaluated following the standard model for metal-oxide semiconductor field-effect transistors.

3. Results and discussion

3.1. Characterization of SnO_x films

XRD patterns for the as-grown SnO_x films fabricated using SnO_x and Sn targets are shown in Fig. 2. The thickness of the SnO_x films was 50 nm. In the pattern for the film deposited using an SnO_x target at P_{O2} = 0 Pa, small broad peaks associated with diffraction from (200), (101), (220), and (211) planes in the tetragonal Sn phase (PDF code: 00–004–0673) are observed. No peaks could be assigned to other phases such as SnO, Sn_2O_3, Sn_3O_4, and SnO_2. These peaks for the Sn phase disappear as P_{O2} increases above 0.017 Pa, indicating that the SnO_x films have an amorphous structure. However, strong sharp peaks due to the Sn phase are observed even at a P_{O2} of 0.025 Pa and are maintained in the patterns for the SnO_x films prepared with P_{O2} as high as 0.05 Pa using the Sn target. An amorphous structure is formed at P_{O2} = 0.26 Pa. The difference in the amounts of Sn formed in the SnO_x films is attributed to differences in the oxygen concentration in the target, suggesting that the SnO_x target has an advantage in terms of suppressing the formation of Sn metal.

XPS wide-range spectra (Fig. 3(a)) and Sn 4d core-line spectra of as-grown SnO_x films fabricated using the SnO_x target at P_{O2} = 0, 0.017, and 0.055 Pa (Fig. 3(b)) are shown in Fig. 3. The thickness of the SnO_x films was 10 nm. The Sn 4d signals are deconvoluted into three components. In the deconvolution, the $4d_{3/2}$ and $4d_{5/2}$ spin–orbit components are considered to be doublets of Gaussian peaks. The Sn^0, Sn^{2+}, and Sn^{4+} components are observed at 24, 25.5, and 26.2 eV, respectively; chemical shifts of ~1.5 and ~0.7 eV toward lower binding energy from Sn^{2+} to Sn^0 and from Sn^{4+} to Sn^{2+}, respectively, are also observed. In the spectrum of the film prepared at P_{O2} = 0 Pa, two large peaks due to Sn^{2+} and Sn^{4+} are observed. A small peak associated with Sn^0 is also seen, consistent with the small, broad Sn peak observed in the XRD pattern (Fig. 2(a)). The Sn^0 peak disappears and the Sn^{4+} peak intensity decreases as P_{O2} increases. Fig. 3(c) shows the Sn^0, Sn^{2+}, and Sn^{4+} fractions of the as-grown SnO_x films (10 nm) fabricated using the SnO_x and Sn targets. Each fraction was estimated from the XPS data. SnO_x films with an Sn^{2+} fraction >40 % were obtained at low Po_2 levels. However, to attain an Sn^{2+} fraction >40 % using the Sn target, a high Po_2 of 0.05 Pa was required. This difference is attributed to the oxidation of SnO (Sn^{2+}) into the thermodynamically stable form by external oxygen during sputtering and to the SnO_2 (Sn^{4+}) component increasing with increasing P_{O2} [35]. Therefore, in subsequent experiments, we used an SnO_x target and P_{O2} = 0 Pa to eliminate the effect of oxidation during sputtering.

The PDA process plays a critical role in the crystallization of the as-deposited SnO films, with the PDA atmosphere being particularly important. Raman spectra of as-grown and annealed SnO_x films (10 nm) prepared using the SnO_x target are shown in Fig. 4(a). PDA was carried out at 300 °C for 60 min under different conditions: N_2, LVPDA, and HVPDA. No peaks are observed in the Raman spectrum of the as-grown film. By contrast, the spectra of the films prepared under N_2, LVPDA, and HVPDA show a strong peak at ~220 cm^{-1} and a weak peak at ~120 cm^{-1}; however, no peaks due to Sn_3O_4 or SnO_2 are observed [37]. The peaks at ~120 and ~220 cm^{-1} correspond to the B_{1g} and A_{1g} vibrational modes of SnO, respectively, indicating its crystallization [38].

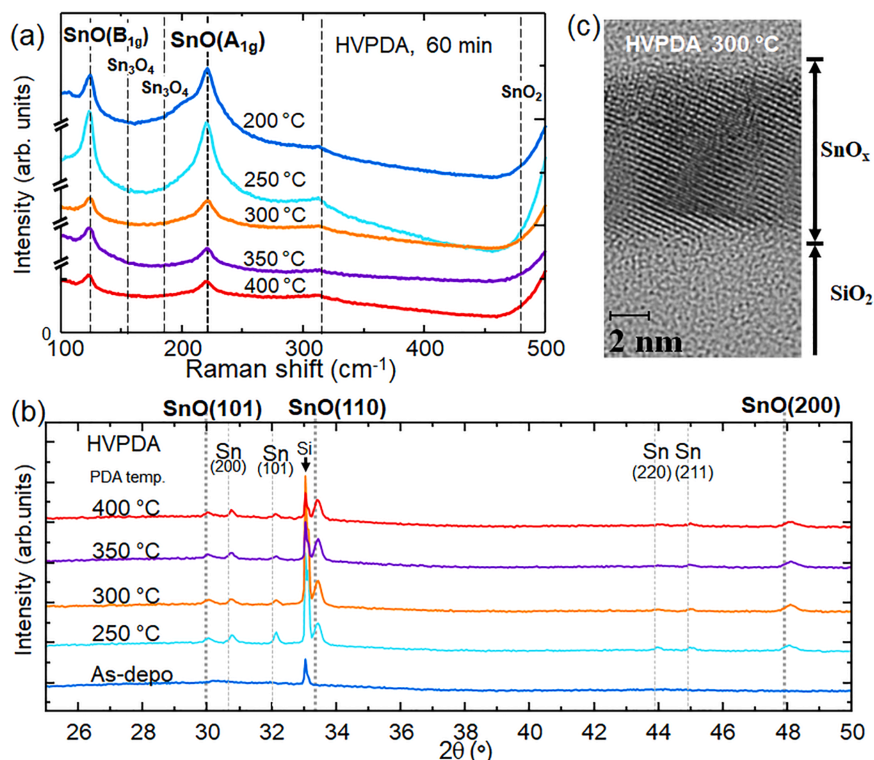

Fig. 5. (a) Raman spectra of SnO_x films after HVPDA at 200–400 °C. (b) XRD patterns of SnO films with a thickness of 50 nm. (c) High-resolution cross-sectional TEM image of SnO_x films after HVPDA at 300 °C.

We carried out XPS analyses (Fig. 4(b) and 4(c)) to evaluate the Sn^0, Sn^{2+}, and Sn^{4+} fractions under different atmospheres. Fig. 4(c) shows the Sn 4d XPS spectra of the as-grown film and the films annealed under N_2, LVPDA, and HVPDA conditions. The Sn^{2+} fraction for the HVPDA film is substantially higher than those for the films annealed under N_2 and LVPDA conditions. The Sn^0, Sn^{2+}, and Sn^{4+} fractions are summarized in Fig. 4(d). The films annealed under N_2 and LVPDA conditions maintained the same Sn^{2+} and Sn^{4+} fractions as the as-grown film. The HVPDA film showed a maximum Sn^{2+} fraction greater than 62 % and a Sn^{2+}/Sn^{4+} ratio greater than 1.6. Here, we express this unintelligible result: although the Sn^{4+} fraction was clearly detected in XPS analysis, SnO_2 binding signal has not been obtained in Raman spectroscopy (Fig. 4(a)). Then, it is difficult to find unified interpretation of this issue at moment.

The presence of excess oxygen has been reported to lead to the transformation of metastable SnO to stable SnO_2 as a result of a local disproportionate redistribution of internal oxygen [39]. The as-grown SnO_x film (10 nm) had an amorphous structure (results not shown). This amorphous film is speculated to be composed of a network of Sn^0, Sn^{2+}, and Sn^{4+}. The film was partially crystallized with the SnO (Sn^{2+}) structure during PDA, as determined from the Raman results in Fig. 4(a). In addition, the Sn^{2+} fraction in the N_2 film slightly increased compared with that in the as-grown film because Sn metal transforms to SnO by acquiring oxygen from the nearest SnO_2. Under an O_2 atmosphere, the oxidation of Sn to SnO_2 via reaction (1) occurs rather than the oxidation of Sn to SnO via reaction (2) [40]:

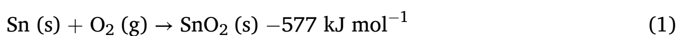

$$\mathrm{Sn\ (s) + O_2\ (g) \rightarrow SnO_2\ (s)\ -577\ kJ\ mol^{-1}} \quad (1)$$

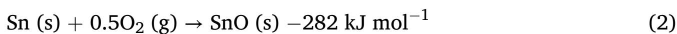

$$\mathrm{Sn\ (s) + 0.5O_2\ (g) \rightarrow SnO\ (s)\ -282\ kJ\ mol^{-1}} \quad (2)$$

It was reported that an oxygen-free atmosphere during PDA was found to be a key factor for the formation of SnO from Sn. With increasing vacuum level, the Sn^{2+} fraction increased, possibly because of accelerated decomposition of the Sn^{4+} network. Chetri et al. reported that surface oxygen vacancies are easily formed in as-prepared SnO_2 under vacuum annealing and that SnO_2 compensates for these oxygen vacancies by transforming itself into SnO [41]. This hypothesis is supported by the experimental observations that the phase transition from SnO_2 to SnO occurs through removal of bridging oxygen atoms from a stoichiometric SnO_2 surface [26]. Therefore, the increase in the SnO fraction after HVPDA was found to involve decomposition of the SnO_2 network. Thus, HVPDA is a suitable annealing process for SnO formation.

The influence of the annealing temperature during HVPDA on SnO crystallization was examined. Fig. 5(a) shows Raman spectra of the SnO_x films (10 nm) after HVPDA at 200–400 °C. Raman spectroscopic analysis confirmed that SnO crystallized at all of the investigated temperatures, and other phases were not detected. We attempted to probe the XRD pattern of the 10 nm thick SnO_x films, but the films were too thin to detect any peaks with our facility. Thus, 50 nm thick films were used to obtain the XRD patterns, which are shown in Fig. 5(b), and also confirmed that no other phases were present. By the way, although the Raman peak intensity of the SnO film annealed at 200 °C is high, it is broadened towards lower wavenumbers with a large full width at half maximum (FWHM) of 29 cm^{-1}, indicating small grain size. In contrast, the peak of the film annealed at 300 °C shows a smaller FWHM of 19 cm^{-1}, indicating better crystal quality. The polycrystalline structure formed at 300 °C was also confirmed by cross-sectional transmission electron microscopy observations (Fig. 5(c)).

3.2. Electrical properties of SnO_x films

The electrical properties of 10-nm-thick SnO_x films annealed under N_2, LVPDA, and HVPDA conditions were first examined using Hall effect measurements. The HVPDA film exhibited p-type conductivity with moderate Hall mobility, whereas the N_2 and LVPDA films showed n-type conductivity (results not shown). This n-type behavior is primarily attributed to a high SnO_2 content, consistent with the XPS results in Fig. 4(c). Corresponding to the XPS data, we found that the Sn^{2+}/Sn^{4+} ratio determines the conduction type, where a ratio greater than 1 is the

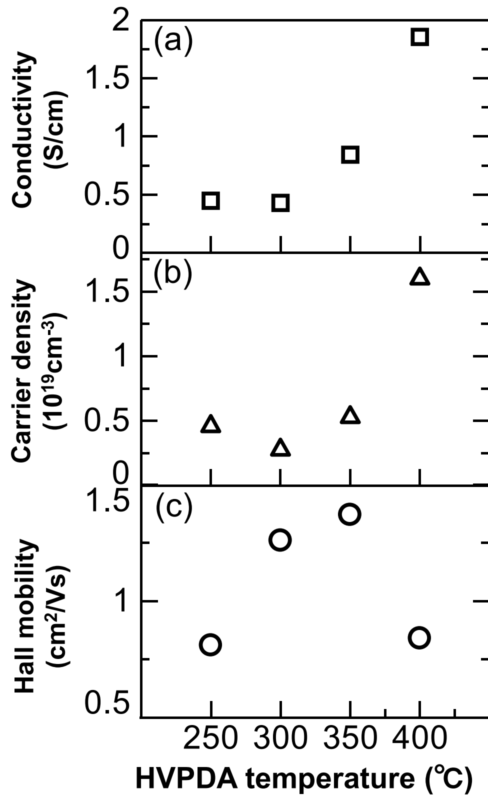

Fig. 6. Conductivity, carrier density, and Hall mobility of SnO_x films after HVPDA at 200–400 °C, as characterized using Hall effect measurements.

criterion for p-type SnO formation.

Fig. 6 shows the conductivity, carrier density, and mobility of the SnO_x films (10 nm) after HVPDA, as evaluated using Hall effect measurements. No conductivity was observed in the SnO_x film subjected to HVPDA at 200 °C. In contrast, p-type behavior was observed in films annealed at a wide range of temperatures from 250 to 400 °C. The conductivity, carrier density, and Hall mobility were 0.5–1.8 S/cm, (0.3–1.6) × 10^{19} cm^{-3}, and 0.8–1.4 cm^2/(V·s), respectively. Increases in the conductivity and carrier density and a reduction of the Hall mobility were observed after HVPDA at 400 °C, suggesting that n-type components (e.g., intermediate oxides and Sn metal) might be incorporated in the p-type SnO channel. This result potentially means that high-temperature HVPDA at 400 °C may lead to a transformation from SnO to other uncontrollable oxides of SnOx and Sn metal, or self-compensating defects, such as oxygen vacancies at high temperatures, may form in the film [42]. Intermediate oxides have been reported to be formed via thermal decomposition of SnO [43].

We fabricated staggered bottom-gate TFTs using SnO films subjected to HVPDA and measured their electrical properties in the dark under vacuum conditions. Fig. 7(a) shows the transfer (I_D–V_G) characteristics of the TFTs fabricated with SnO channels subjected to various PDA temperatures. The V_{DS} was maintained at −0.1 V. p-Type behavior was observed for all of the TFTs, as indicated by the increase in I_{DS} with increasingly negative V_G. The output (I_D–V_D) characteristics of the TFT fabricated at 300 °C show linear and saturation regions (Fig. 7(b)). The linear region indicates that the Ni contacts form an ohmic contact with the SnO channels. The contact resistance, extracted using the transmission line method (TLM; channel length of 50–350 μm), was estimated to be in the range from 10^2 to 10^3 Ω·cm. Parameters such as the linear-region field effect mobility (μ_{FE}), subthreshold sing (*SS*), on-off current change (I_{on}/I_{off}) ratio, and threshold voltage (V_{TH}) were extracted from the transfer characteristics; the extracted values are plotted in Fig. 7(c). Relatively high μ_{FE} values greater than 1.8 cm^2/(V·s), small *SS* values of 10 V/dec, and high I_{on}/I_{off} ratios greater than 3.5 × 10^4 were maintained at 250–300 °C. These properties were degraded when the HVPDA temperature was increased to 350 or 400 °C. The *SS* value is known to depend on the trap density in the interface between an SiO_2 dielectric and an SnO channel. A trade-off relationship

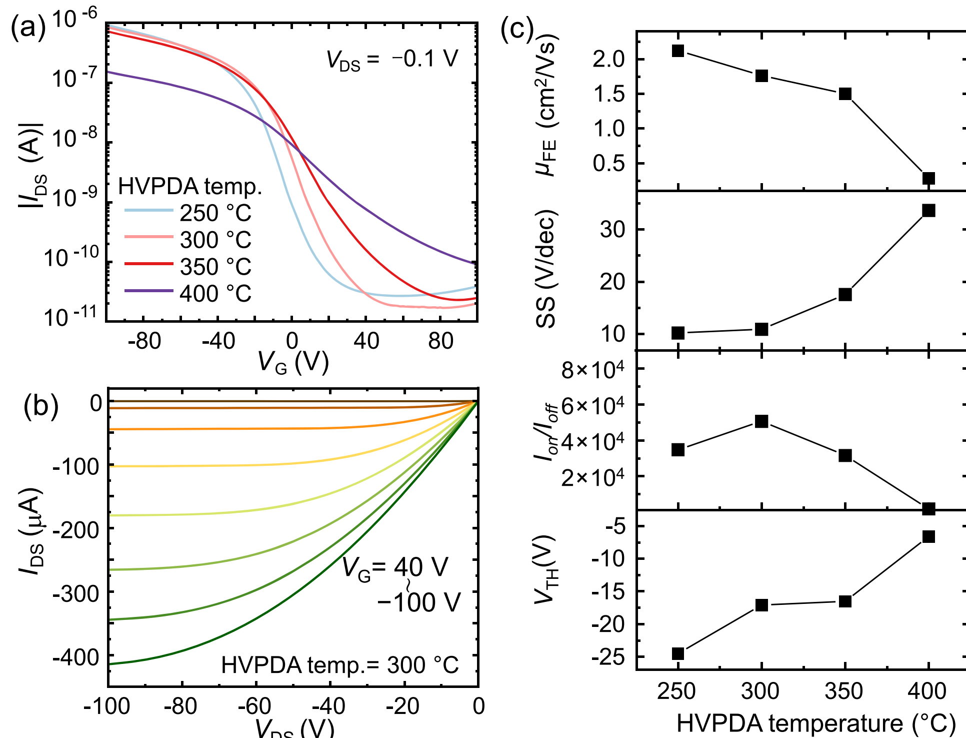

Fig. 7. (a) I_d–V_g at V_{DS} of −0.1 V, (b) I_d–V_d at 300 °C, and (c) mobility, *SS*, I_{on}/I_{off}, and V_{TH} properties of bottom-gate TFTs with SnO channel (channel length = 250 μm, width = 1000 μm).

between SS and μ_{FE} with respect to the HVPDA temperature was clearly observed, indicating that the trap density at the SiO_2/SnO interface increased as a function of HVPDA temperature. The V_{TH} value shifted in the positive direction as the HVPDA temperature increased, indicating that electron traps were formed in the SiO_2/SnO structure of the TFT. One of the origins of these phenomena is that n-type components were incorporated into the p-type SnO channel. The I_{off} current, which corresponds to electron transfer in the accumulation region, was substantially smaller in the films annealed at 300 °C than in those annealed at 250 °C (Fig. 7(a)). The large I_{off} current in the film annealed at 250 °C is attributed to insufficient transformation from SnO_2 to SnO as a result of low-temperature HVPDA. We found that the optimal HVPDA temperature to obtain stable p-type SnO is 300 °C. The relatively high μ_{FE} of 1.8 $cm^2/(V{\cdot}s)$ and high I_{on}/I_{off} ratio of 5.1×10^4 are comparable to previously reported values [19,21,44]. Therefore, HVPDA at the optimal temperature is clearly a suitable method to increase the p-type SnO fraction.

4. Conclusion

The effects of the PDA atmosphere and temperature on the SnO fraction in SnO_x films were investigated. As-grown SnO_x films deposited by RF sputtering using an SnO_x (SnO:Sn = 60:40) target had an SnO (Sn^{2+}) fraction of 42 % even when deposited at $P_{O2} = 0$ Pa. HVPDA ($<5 \times 10^{-4}$ Pa) was found to substantially increase the Sn^{2+}component to 62 % and induce p-type behavior, unlike PDA conducted under N_2 and low-vacuum (~1 Pa) conditions, which resulted in n-type behavior. This p-type behavior was attributed to the transformation from SnO_2 to SnO during HVPDA. For staggered bottom-gate TFTs with an SnO channel, HVPDA at temperatures ranging from 200 to 400 °C consistently led to p-type characteristics, with the best performance observed for the device corresponding to HVPDA at 300 °C, where the resultant film exhibited an I_{on}/I_{off} ratio of 5.1×10^4 and a μ_{FE} of 1.8 $cm^2/(V{\cdot}s)$. Our investigation into the critical parameters for achieving high-performance p-type TFTs provides valuable insights for optimizing SnO sputtering and PDA processes.

CRediT authorship contribution statement

Yong-Lie Sun: Writing – original draft, Investigation, Data curation. **Toshihide Nabatame:** Writing – review & editing, Writing – original draft, Supervision, Investigation, Conceptualization. **Jong Won Chung:** Writing – review & editing, Investigation, Conceptualization. **Tomomi Sawada:** Data curation. **Hiromi Miura:** Data curation. **Manami Miyamoto:** Data curation. **Kazuhito Tsukagoshi:** Writing – review & editing, Writing – original draft, Supervision, Investigation, Conceptualization.

Declaration of competing interest

The authors declare the following financial interests/personal relationships which may be considered as potential competing interests:

Kazuhito Tsukagoshi reports financial support was provided by SAIT. If there are other authors, they declare that they have no known competing financial interests or personal relationships that could have appeared to influence the work reported in this paper.

Acknowledgments

Part of this work was performed under the Cooperative Research Program of Institute for Joining and Welding Research Institute, Osaka University. This research was supported by the Samsung Advanced Institute of Technology (SAIT).

Data availability

No data was used for the research described in the article.

References

[1] K. Nomura, H. Ohta, A. Takagi, T. Kamiya, M. Hirano, H. Hosono, Room-temperature fabrication of transparent flexible thin-film transistors using amorphous oxide semiconductors, Nature 432 (2004) 488–492, https://doi.org/10.1038/nature03090.

[2] E. Fortunato, P. Barquinha, R. Martins, Oxide semiconductor thin-film transistors: a review of recent advances, Adv. Mater. 24 (2012) 2945–2986, https://doi.org/10.1002/adma.201103228.

[3] S. Parthiban, J.Y. Kwon, Role of dopants as a carrier suppressor and strong oxygen binder in amorphous indium-oxide-based field effect transistor, J. Mater. Res. 29 (2014) 1585–1596, https://doi.org/10.1557/jmr.2014.187.

[4] S. Aikawa, T. Nabatame, K. Tsukagoshi, Si-incorporated amorphous indium oxide thin-film transistors, Jpn. J. Appl. Phys. 58 (2019), https://doi.org/10.7567/1347-4065/ab2b79, 090506-1-09056-15.

[5] D. Kwon, E.C. Park, W. Shin, R.H. Koo, J. Hwang, J.H. Bae, D. Kwon, J.H. Lee, Analog synaptic devices based on IGZO thin-film transistors with a metal-ferroelectric-metal-insulator-semiconductor structure for high-performance neuromorphic systems, Adv. Intell. Syst. 5 (2023) 2300125, https://doi.org/10.1002/aisy.202300125.

[6] M. Si, Z. Lin, Z. Chen, X. Sun, H. Wang, P.D. Ye, Scaled indium oxide transistors fabricated using atomic layer deposition, Nat. Electron. 5 (2022) 164–170, https://doi.org/10.1038/s41928-022-00718-w.

[7] R. Kobayashi, T. Nabatame, T. Onaya, A. Ohi, N. Ikeda, T. Nagata, K. Tsukagoshi, A. Ogura, Comparison of characteristics of thin-film transistor with In2O3 and carbon-doped In2O3 channels by atomic layer depostion and post-metallization annealing in O3, Jpn. J. Appl. Phys. 60 (201) 030903, doi:10.35848/1347-4065/abde54.

[8] S. Aikawa, T. Nabatame, K. Tsukagoshi, Effects of dopants in InOx-based amorphous oxide semiconductors for thin-film transistor applications, Appl. Phys. Lett. 103 (2013), https://doi.org/10.1063/1.4822175, 172105-1-172105-5.

[9] N. Mitoma, S. Aikawa, X. Guo, T. Kizu, M. Shimizu, M.F. Lin, T. Nabatame, K. Tsukagoshi, Stable amorphous In_2O_3-based thin-film transistors by incorporating SiO_2 to suppress oxygen vacancies, Appl. Phys. Lett. 104 (2014), https://doi.org/10.1063/1.4868303, 102103-1-102103-5.

[10] Y. Zhang, G. He, L. Wang, W. Wang, X. Xu, W. Liu, Ultraviolet-assisted low-thermal-budget-driven α-InGaZnO thin films for high-performance transistors and logic circuits, ACS Nano 16 (2022) 4961–4971, https://doi.org/10.1021/acsnano.2c01286.

[11] Z.W. Shang, Hs.H. Hsu, Z.W. Zheng, C.H. Cheng, Progress and challenges in p-type oxide-based thin film transistors, Nanotechnol. Rev. 8 (2019) 422–443, https://doi.org/10.1515/ntrev-2019-0038.

[12] G. Byeon, S.C. Jang, T. Roh, J.M. Park, H.S. Kim, Y.Y. Noh, Recent progress in the development of backplane thin film transistors for information displays, J. Inf. Disp. 24 (2023) 159–168, https://doi.org/10.1080/15980316.2023.2219030.

[13] L.Y. Liang, Z.M. Liu, H.T. Cao, Z. Yu, Y.Y. Shi, A.H. Chen, H.Z. Zhang, Y.Q. Fang, X. L. Sun, Phase and optical characterizations of annealed SnO thin films and their p-type TFT application, J. Electrochem. Soc. 157 (2010) H598–H602, https://doi.org/10.1149/1.3385390.

[14] L.Y. Liang, H.T. Cao, X.B. Chen, Z.M. Liu, F. Zhuge, H. Luo, J. Li, Y.C. Lu, W. Lu, Ambipolar inverters using SnO thin-film transistors with balanced electron and hole mobilities, Appl. Phys. Lett. 100 (2012), https://doi.org/10.1063/1.4731271, 263502-1-263502-5.

[15] H. Luo, L.Y. Liang, Q. Liu, H.T. Cao, Magnetron-sputtered SnO thin films for p-type and ambipolar TFT applications, ECS J. Solid State Sci. Technol. 3 (2014) Q3091–Q3094, https://doi.org/10.1149/2.017409jss.

[16] S.H. Kim, I.H. Baek, D.H. Kim, J.J. Pyeon, T.M. Chung, S.H. Baek, J.S. Kim, J. H. Han, S.K. Kim, Fabrication of high-performance p-type thin film transistors using atomic-layer-deposited SnO films, J. Mater. Chem. C 5 (2017) 3139–3145, https://doi.org/10.1039/C6TC04750E.

[17] Y. Zhou, Y. Song, R. Hong, X. Liu, X. Zou, B. Iníguez, D. Flandre, G. Li, L. Liao, Electrical evolution of p-type SnO_x film and transistor deposited by RF magnetron sputtering, IEEE Trans. Electron Dev. 70 (2023) 3100–3105, https://doi.org/10.1109/TED.2023.3266417.

[18] E. Fortunato, R. Barros, P. Barquinha, V. Figueiredo, S.H.K. Park, C.S. Hwang, R. Martins, Transparent p-type SnO_x thin film transistors produced by reactive rf magnetron sputtering followed by low temperature annealing, Appl. Phys. Lett. 97 (2010), https://doi.org/10.1063/1.3469939, 052105-1-052105-3.

[19] J.A. Caraveo-Frescas, P.K. Nayak, H.A. Al-Jawhari, D.B. Granato, U. Schwingenschlögl, H.N. Alshareef, Record mobility in transparent p-type tin monoxide films and devices by phase engineering, ACS Nano 7 (2013) 5160–5167, https://doi.org/10.1021/nn400852r.

[20] H. Yabuta, N. Kaji, R. Hayashi, H. Kumomi, K. Nomura, T. Kamiya, M. Hirano, H. Hosono, Sputtering formation of p-type SnO thin-film transistors on glass toward oxide complimentary circuits, Appl. Phys. Lett. 97 (2010), https://doi.org/10.1063/1.3478213, 072111-1-072111-3.

[21] K.H. Bae, M.G. Shin, S.H. Hwang, H.S. Jeong, D.H. Kim, H.I. Kwon, Electrical performance and stability improvement of p-channel SnO thin-film transistors using atomic-layer-deposited Al_2O_3 capping layer, IEEE Access 8 (2020) 222410–222416, https://doi.org/10.1109/ACCESS.2020.3043780.

[22] M. Batzill, U. Diebold, The surface and materials science of tin oxide, Prog. Surf. Sci. 79 (2005) 47–154, https://doi.org/10.1016/j.progsurf.2005.09.002.

[23] Y. Li, Q. Xin, L. Du, Y. Qu, H. Li, X. Kong, Q. Wang, A. Song, Extremely sensitive dependence of SnO_x film properties on sputtering power, Sci. Rep. 6 (2016), https://doi.org/10.1038/srep36183, 36183-1-36183-9.

[24] A. Nikiforov, V. Timofeev, V. Mashanov, I. Azarov, I. Loshkarev, V. Voodin, D. Gulyaev, I. Ghetyrin, I. Korolkov, Formation of SnO and SnO_2 phases during the annealing of SnO(x) films obtained by molecular beam epotaxy, Appl. Surf. Sci. 512 (2020), https://doi.org/10.1016/j.apsusc.2020.145735, 145735-1-145735-7.

[25] P. Sarker, M.N. Huda, Understanding the thermodynamic pathways of SnO-to-SnO_x phase transition, Compt. Mater. Sci. 111 (2016) 359–365, https://doi.org/10.1016/j.commatsci.2015.09.041.

[26] M. Batzill, K. Katsiev, J.M. Burst, U. Diebold, Gas-phase-dependent properties of SnO_2 (110), (100), and (101) single-rystal surface: Structure, composition, and electronic properties, Phys. Rev. B 72 (2005), https://doi.org/10.1103/PhysRevB.72.165414, 165414-1-16514-20.

[27] H. Luo, L.Y. Liang, H.T. Cao, Z.M. Liu, F. Zhuge, Structural, chemical, optical, and electrical evolution of SnO_x films deposited by reactive RF magnetron sputtering, ACS Appl. Mater. Interfaces. 4 (2012) 5673–5677, https://doi.org/10.1021/am301601s.

[28] T. Toyama, Y. Seo, T. Konishi, H. Okamoto, Y. Tsutsumi, Physical properties of p-type tin monoxide films deposited at low temperature by radio frequency magnetron sputtering, Appl. Phys. Express 4 (2011), https://doi.org/10.1143/APEX.4.071101, 071101-1-071101-3.

[29] P.C. Hsu, C.C. Wu, H. Hiramatsu, T. Kamiya, H. Hosono, Film texture, hole transport and field-effect mobility in polycrystalline SnO thin films on glass, ECS J. Solid State Sci. Technol. 3 (2014) Q3040–Q3044, https://doi.org/10.1149/2.009409jss.

[30] C.K.G. Kwok, Y. Wang, X. Shu, K.M. Yu, Conversion of p-type SnO to n-type SnO_2 via oxidation and the band offset and rectification of an all-Tin oxide p-n junction structure, Appl. Surf. Sci. 627 (2023), https://doi.org/10.1016/j.apsusc.2023.157295, 157295-1-157295-7.

[31] P.C. Hsu, C.J. Hsu, C.H. Chang, S.P. Tsai, W.C. Chen, H.H. Hsieh, C.C. Wu, Sputtering deposition of p-type SnO films with SnO_2 target in hydrogen-containing atmosphere, ACS Appl. Mater. Interfaces 6 (2014) 13724–13729, https://doi.org/10.1021/am5031787.

[32] S.S. Lin, S.Y. Hfan, Y.S. Tsai, Effects of annealing on wettability and physical properties of SnO thin films deposited at low RF power densities, Ceram. Int. 43 (2017) 1802–1808, https://doi.org/10.1016/j.ceramint.2016.10.138.

[33] P.C. Hsu, W.C. Chen, Y.T. Tsai, Y.C. Kung, C.H. Chang, C.C. Wu, H.H. Hsieh, Sputtering deposition of P-type SnO films using robust Sn/SnO_2 mixed target, Thin Solid Films 555 (2014) 57–61, https://doi.org/10.1016/j.tsf.2013.06.059.

[34] P.C. Hsu, S.P. Tsai, C.H. Chang, C.J. Hsu, W.C. Chen, H.H. Hsieh, C.C. Wu, Preparation of p-type SnO thin films and transistors by sputtering with robust Sn/SnO_2 mixed target in hydrogen-containing atmosphere, Thin Solid Films 585 (2015) 50–56, https://doi.org/10.1016/j.tsf.2015.04.034.

[35] C. Kim, S. Cho, S. Kim, S.E. Kim, Comparative analysis of SnO_x thin films deposited by RF reactive sputtering with different SnO/Sn target compositions, ECS J. Solid State Sci. Technol. 6 (2017) 765–771, https://doi.org/10.1149/2.0061712jss.

[36] L. Pan, W. Li, S.E. Yang, J. Zang, H. Guo, T. Xia, W. Shen, Y. Chen, Effects of annealing conditions on the properties of SnO films deposited by e-beam evaporation process, Mater. Lett. 257 (2019) 1267371–1267371-4, https://doi.org/10.1016/j.matlet.2019.126737.

[37] B. Eifert, M. Becker, C.T. Reindl, M. Giar, L. Zheng, A. Polity, Y. He, C. Heilliger, P. J. Klar, Raman studies of the intermediate tin-oxide phase, Phy. Rev. Mater. 1 (2017), https://doi.org/10.1103/PhysRevMaterials.1.014602, 014602-1-014602-6.

[38] J. Geurts, S. Rau, W. Richter, F.J. Schmitte, SnO films and their oxidation to SnO_2: Raman scattering, IR reflectivity nd x-ray diffraction studies, Thin solid Films 121 (1984) 217–225.

[39] X.Q. Pan, L. Fu, Oxidation and phase transitions of epitaxial tin oxide thin films on (1012) sapphire, J. Appl. Phys. 89 (2001) 6048–6055.

[40] A.Y. Mohamed, S.J. Lee, Y. Jang, J.S. Kim, C.S. Hwang, D.Y. Cho, X-ray spectroscopy study on the electronic structure of Sn-added p-type SnO films, J. Phys.: Condens. Matter. 32 (2020) 065502, https://doi.org/10.1088/136-1648X/ab4f51.

[41] R. Chetri, B. Choudhury, A. Choudhury, Room temperature ferromagnetism in SnO_2 nanoparticles: as experimental and density functional study, J. Mater. Chem. C. 2 (2014) 9294–9302, https://doi.org/10.1039/c4tc01070a.

[42] G.K. Deyu, J. Hunka, H. Roussel, J. Brötz, D. Bellet, A. Klein, Electrical properties of low-temperature processed Sn-doped In2O3 thin films: the role of microstructure and oxygen content and the potential of defect modulation doping, Materials 12 (2019) 2232, https://doi.org/10.3390/ma12142232.

[43] M.S. Moreno, R.C. Mercader, A.G. Bibiloni, Study of intermediate oxides in SnO thermal decomposition, J. Phys.: Condens. Matter. 4 (1992) 351–355, https://doi.org/10.1063/1.4822175.

[44] Y. Ogo, H. Hiramatsu, K. Nomura, H. Yanagi, T. Kamiya, M. Hirano, H. Hosono, p-Channel thin-film transistor using p-type oxide semiconductor, SnO, Appl. Phys. Lett. 93 (2008), https://doi.org/10.1063/1.2964197, 032113-1-032113-3.